

1 **Electron fluxes at geostationary orbit from GOES MAGED data**

2 **I. Sillanpää,¹N. Yu. Ganushkina,^{1,2}S. Dubyagin,¹and J. V. Rodriguez³**

3 ¹Finnish Meteorological Institute, Helsinki, Finland.

4 ²University of Michigan, Ann Arbor, MI, USA.

5 ³Cooperative Institute for Research in Environmental Sciences, University of Colorado Boulder, Boulder, Colorado, USA.

6 **Key Points:**

- 7 • An empirical, predictive model function is presented for electron fluxes for energies
8 of 40, 75, and 150 keV at geostationary orbit.
- 9 • Higher solar wind speed in general and negative IMF B_Z at midnight to noon result
10 in electron flux enhancements in energies 30–200 keV at geostationary orbit.

This is the author manuscript accepted for publication and has undergone full peer review but has not been through the copyediting, typesetting, pagination and proofreading process, which may lead to differences between this version and the [Version of Record](#). Please cite this article as doi: [10.1002/2017SW001698](https://doi.org/10.1002/2017SW001698)

Corresponding author: Ilkka Sillanpää, ilkka.sillanpaa@fmi.fi

Abstract

Electron behavior in energies below 200 keV at geostationary orbit has significance for satellite operations due to charging effects on spacecraft. Five years of keV energy electron measurements by the geostationary GOES-13 satellite's MAGED instrument have been analyzed. A method for determining flight-direction integrated fluxes is presented. The electron fluxes at the geostationary orbit are shown to have significant dependence on solar wind speed and IMF B_Z : increased solar wind speed correlates with higher electron fluxes with all magnetic local times while negative IMF B_Z increases electron fluxes in the 0 to 12 MLT sector. A predictive empirical model for electron fluxes in the geostationary orbit for energies 40, 75, and 150 keV was constructed and is presented here. The empirical model is dependent on three parameters: magnetic local time, solar wind speed, and IMF B_Z .

1 Introduction

The populations of low energy electrons (below 200–300 keV) and their variations in the Earth's inner magnetosphere are critically important for the magnetospheric dynamics. One of their obvious roles is being a seed population, further accelerated to MeV energies by various processes in the Earth's radiation belts [Horne *et al.*, 2005; Chen *et al.*, 2007; Turner and Li, 2008; Li *et al.*, 2014; Jaynes *et al.*, 2015; Boyd *et al.*, 2016]. Another important effect is that the low-energy electron flux is highly responsible for surface charging effects on satellites [Garrett, 1981; Lanzerotti *et al.*, 1998; Davis *et al.*, 2008; Thomsen *et al.*, 2013]. Recently Ma *et al.* [2016] showed with their simulation study that the scattering of low-energy electrons by chorus waves together with intense electric field spikes lead to higher fluxes in energies 10–100 keV in the outer radiation belt indicating an important source mechanism for keV electrons.

There have been some long-time and even continuous measurements of low energy electrons and ions by satellites in geosynchronous or geostationary orbits. Numerous studies have been published on the analysis and modeling based on these measurements as described below.

Early measurements made by geostationary satellites ATS-1 and 1976-059A (DPS F6) revealed general features through statistical studies (Lezniak and Winckler [1970]; Baker *et al.* [1978]). In addition, the variations of electron anisotropies in keV energies

42 were associated with geomagnetic activity and the flattening of the electron pitch-angle
43 distributions during substorm onsets in the night sector.

44 *Korth et al.* [1999] presented statistics for one year of proton and electron fluxes at
45 geosynchronous orbit measured by three LANL satellites, using the data from the Magne-
46 tospheric Plasma Analyzer (MPA) instrument which covered the energy range from 1 eV/q
47 to 40 keV/q [*Bame et al.*, 1993; *McComas et al.*, 1993]. Organized as a function of the lo-
48 cal time and the Kp index, the fluxes show distinct boundaries which were interpreted to
49 be caused by global magnetospheric particle drifts in the presence of loss processes due
50 to charge-exchange of the ions and auroral precipitation of the electrons. The following
51 study by *Korth and Thomsen* [2001] further confirmed that obtained statistical boundaries
52 approximately match the Alfvén boundary crossings when calculated using simple repre-
53 sentations of convective electric field [*Volland*, 1973; *Stern*, 1975] and dipole magnetic
54 field.

55 *Shi et al.* [2009] statistically examined the geosynchronous energetic flux response as
56 measured by LANL SOPA to solar wind dynamic pressure enhancements. It was obtained
57 that for low-energy electrons, the primary response to magnetospheric compression is an
58 increase in flux at geosynchronous orbit. *Li et al.* [2005] found using daily solar wind and
59 IMF data that solar wind speed enhancements result in higher electron fluxes at geosyn-
60 chronous orbit; the optimal time delay was found to increase rapidly with energy from a
61 couple of hours or less for 50–150 keV to 15–25 hours for energies 250 keV and above.

62 *Denton et al.* [2005] and *Thomsen et al.* [2007] presented the LANL geosynchronous
63 data set extended to more than a full solar cycle. *Denton et al.* [2005] identified depen-
64 dencies in the average plasma properties at the geosynchronous orbit by studying MPA
65 instrument data with respect to the Dst index, local time, storm phase, and solar cycle.
66 For electrons their energy range was from 30 eV to about 45 keV. For low Kp indexes
67 the electron density is typically highest in the midnight-dawn sector while for Kp>7 the
68 electron density becomes high throughout the geosynchronous orbit. For electron temper-
69 atures, however, the largest average values are in the midnight-dawn sector, and were not
70 found to expand any further for higher Kp values beyond the extent found at Kp=4. *Thom-*
71 *sen et al.* [2007] gave percentile values for particle fluxes in energies from 1 eV to 40 keV;
72 particularly, the lowest measured energy electron and proton fluxes were even orders of
73 magnitude larger than by the ATS-6 model used in satellite design.

74 *Sicard-Piet et al.* [2008] created a model for yearly electron fluxes between 1 keV
75 and 5.2 MeV at the geostationary orbit by combining multiple satellite data sets; its usability
76 is especially towards estimating charged particle doses for spacecraft and solar panel
77 degradation. Another type of empirical model was created by *Denton et al.* [2015] from
78 LANL geosynchronous satellite data using MPA instruments for energies from about 1 eV
79 to 40 keV. The model provides flux probabilities as percentile values for given Kp index,
80 magnetic local time (MLT), and solar activity index $F_{10.7}$ values. *Kellerman and Shprits*
81 [2012] determined two-dimensional probability distributions functions dependent on solar
82 wind speed and density using electron data from the LANL geosynchronous satellites in
83 energies between 20 keV and 3.5 MeV. Their results showed that electron fluxes have a
84 positive correlation with the solar wind speed while mid-to-high energy fluxes show anti-
85 correlation with the solar wind density.

86 *Hartley et al.* [2014] used MAGED 30–600 keV electron data of year 2011 from the
87 GOES-13 geostationary satellite to determine the effect of solar wind speed and density
88 on the electron density, temperature and energy density at the geostationary orbit. They
89 found that simultaneously elevated electron number density and temperature are usually
90 preceded by fast solar wind speed about 24 hours previous. They also presented predictive
91 formulas for electron density, temperature and energy density at geostationary orbit; espe-
92 cially, the electron density lower limit shows dependence on the solar wind speed from 12
93 to 48 hours in advance.

94 There have been also studies focusing on the effects of high-speed solar wind events.
95 In their study using over a hundred superposed high-speed-stream epochs, *Denton and*
96 *Borovsky* [2008] analyzed plasma behavior on the dayside geosynchronous orbit. It was
97 found that magnetospheric convection is increased creating very dense plasma at geosyn-
98 chronous orbit about 20 hours after the convection onset. *Turner et al.* [2016] have used
99 new observations of a substorm activity event by the Magnetospheric Multiscale mission
100 and they found that there was an upper energy cutoff for electron acceleration by betatron
101 and Fermi mechanisms that increased from 130 to over 500 keV over five or more injec-
102 tions.

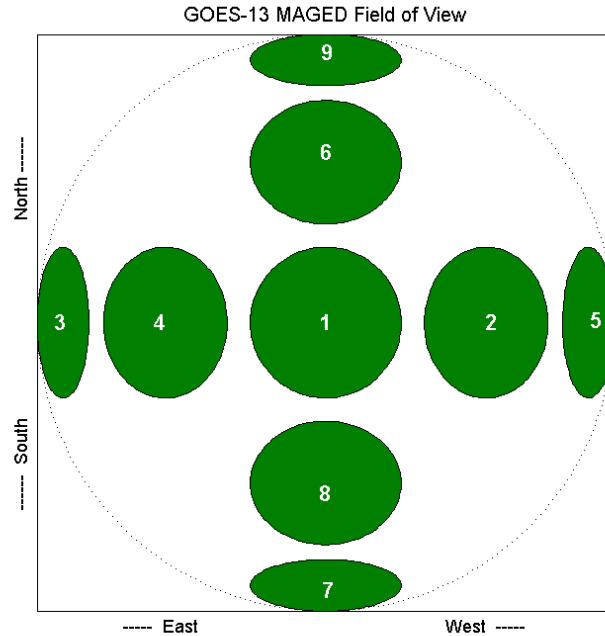
103 The studies cited above show the dynamic nature of the keV energy range elec-
104 trons at geosynchronous orbit and how the understanding of their behavior and also de-
105 pendence on various magnetospheric processes has increased over the past decade or so.

106 While many studies have shown correlations between solar wind conditions and energetic
107 plasma features within Earth's magnetosphere, it should be emphasized that it is through a
108 chain of processes that the solar wind affects, for example, electron flux enhancements at
109 geosynchronous orbit. Namely, substorm injections and enhancements in magnetospheric
110 convection and convection electric field are among the key mechanisms that directly af-
111 fect energetic plasma in the inner magnetosphere and at geosynchronous orbit. It is in this
112 context that our current study is taking a statistical look on the correlations between so-
113 lar wind and interplanetary magnetic field and electrons at geosynchronous orbit in the
114 10's to 100's of keV energy range. Our purpose is to create a predictive empirical model
115 for plasma conditions of low-energy electrons at geosynchronous orbit. We are building
116 a model dependent only on parameters observed upstream of Earth. By using only solar
117 wind and interplanetary magnetic field (IMF) parameters for the model and no geomag-
118 netic or magnetospheric indices, we create a predictive model that can be run in real time.

119 The rest of the paper is organized as follows. In Section 2 the GOES-13 MAGED
120 instrument and data used in the study are described along with the method of determining
121 flight-direction integrated fluxes. Then the electron fluxes for a five-year period are orga-
122 nized in Section 3 by solar wind and IMF parameters and analysis results are described.
123 In Section 4 a new empirical model for electron fluxes in the geostationary orbit is pre-
124 sented for energies of 40, 75 and 150 keV along with the steps of its construction. The
125 Discussion and Conclusions section concludes the paper.

126 **2 Flight-direction integrated GOES MAGED data**

127 The MAGED (MAGnetospheric Electron Detector) instrument onboard the GOES-
128 13 satellite is a set of nine collimated solid state detectors [*GOES N Series Data Book*,
129 *Hanser*, 2011; *Rowland and Weigel*, 2012; *Rodriguez*, 2014]. The detectors operate
130 in five energy channels of 30–50 keV, 50–100 keV, 100–200 keV, 200–350 keV, and 350–
131 600 keV for electrons. The nine detectors, or telescopes, each with a full detection cone
132 angle of 30 degrees, form two crossing fans with the central telescope 1 pointing directly
133 away from the Earth. Figure 1 shows their fields of views (numbered green ellipses) as
134 seen from the Earth and situated on a unit sphere projected onto a plane perpendicular to
135 the Earthward direction. The orientation of the spacecraft is nominal in Figure 1.



142 **Figure 1.** The fields of views of the MAGED telescopes (numbered green ellipses) as seen from the Earth
 143 and situated on a unit sphere projected onto a plane perpendicular to the Earthward direction. Telescope 1
 144 points in anti-Earth direction as seen from the Earth. Each telescope has a full detection cone angle of 30
 145 degrees.

136 The MAGED archival flux data is provided as differential electron fluxes determined
 137 for the midpoint of the five energy ranges (i.e., 40, 75, 150, 275, and 475 keV) and given
 138 separately for all nine telescopes. For the present study, we use the first three channels.

139 The GOES-13 satellite is located on geostationary orbit at longitude of 75 degrees west.
 140 GOES-13 has been kept in the nominal orientation since the start of its operation in May
 141 2010.

146 In order to have one representative flux value for each energy instead of nine sepa-
 147 rate values from the nine telescopes, we determine flight-direction integrated differential
 148 electron fluxes for each of the energies 40 keV, 75 keV, and 150 keV. The flight-direction
 149 integrated flux is calculated in the case of the MAGED data similarly how the omnidirec-
 150 tional flux would be but it has an additional factor $\frac{1}{4\pi}$ and consequently also steradian (sr)
 151 in the units. For this, we use the directional differential fluxes of the nine telescopes and
 152 their pitch angles based on the magnetic field measurements by Magnetometer 1 onboard

153 GOES-13. The directional differential electron fluxes and pitch angles for each telescope
154 are provided in the NOAA archival data (available at http://satdat.ngdc.noaa.gov/sem/goes/data/new_avg/).

155 The nine MAGED telescopes do not provide a full coverage of the full solid angle.
156 Indeed, they provide a partial coverage on the hemisphere in the anti-Earthward direc-
157 tion. Furthermore, if the local magnetic field has a significant component along the Earth-
158 satellite line, as when the near-field stretches prior to a particle injection, all the pitch an-
159 gles from 0 to 180 degrees cannot be covered by the telescopes. With this partial solid
160 angle coverage, an integrated flux can still be obtained if we assume that the directional
161 electron fluxes are (1) gyrotropic (i.e., fluxes are uniform in all directions with the same
162 pitch angle) and (2) reflection symmetric with respect to the plane perpendicular to the
163 magnetic field (i.e., fluxes for pitch angles α from 0 to $\pi/2$ are the same as from $\pi/2$ to
164 π , or $J(\pi - \alpha) = J(\alpha)$). Therefore, in order to address the sparseness of samples in pitch-
165 angle space, we replace those pitch angles $\alpha > \frac{\pi}{2}$ with $\pi - \alpha$, an operation we refer to as
166 'folding', resulting in improved sampling between 0 and $\frac{\pi}{2}$. These assumptions represent
167 an ideal case which results from the Liouville's theorem when neither particle accelera-
168 tion nor losses are considered. *Åsnes et al.* [2005] studied peaks in the electron pitch angle
169 distributions at the geosynchronous orbit with LANL satellites in energies up to 47 keV
170 and found the flux peaks consistently very symmetric. Thus, the assumptions seem to be
171 justified for our purposes.

172 The nine MAGED telescopes actually provide a good pitch angle coverage of elec-
173 tron fluxes for any direction of the magnetic field when these two assumptions are ac-
174 cepted, and the calculation of flight-direction integrated flux is simplified. It follows that
175 a flight-direction integrated differential flux J for each energy channel can be determined
176 by using the directional differential electron fluxes of individual telescopes to estimate
177 the differential fluxes in all directions and then integrating these fluxes over the full solid
178 angle of 4π . The flight direction integrated flux in units of $1/(\text{cm}^2 \text{ s sr keV})$ is obtained
179 using the following:

$$\begin{aligned}
J &= \frac{1}{4\pi} \int_{4\pi} J(\Omega) d\Omega \\
&= \frac{1}{4\pi} \cdot 2\pi \cdot 2 \int_0^{\pi/2} J_{\text{folded}}(\alpha) \sin(\alpha) d\alpha \\
&= \sum_{i=1}^n J_i \int_{\alpha_{i0}}^{\alpha_{i1}} \sin(\alpha) d\alpha \\
&= \sum_{i=1}^n J_i [-\cos(\alpha_{i0}) - (-\cos(\alpha_{i1}))]
\end{aligned} \tag{1}$$

$$J_i = \frac{\sin(\alpha_{i0}) \cdot J_{i0} + \sin(\alpha_{i1}) \cdot J_{i1}}{\sin(\alpha_{i0}) + \sin(\alpha_{i1})} \tag{2}$$

Here $J(\Omega)$ is the directional flux as function of the solid angle Ω . J_{i0} is the directional differential flux by a detector at the beginning of a folded pitch angle interval i and J_{i1} is the directional differential flux at the other end of the interval; the corresponding pitch angles are α_{i0} and α_{i1} , respectively.

First, we move from integrating over solid angle Ω to integrating over folded pitch angles α . Using assumption (1), we take the integrated flux over all directions with a given pitch angle α to be the product of the flux for that pitch angle and the circumference of the circle that pitch angle forms in directional space, namely $2\pi \cdot \sin(\alpha)$. Furthermore, assumption (2) gives that the integration over pitch angles from 0 to π is twice the integration over folded pitch angles from 0 to $\pi/2$, and hence we have a factor 4π . Then to discretize the integration over fluxes of the folded pitch angles J_α to the actual pitch angles of the telescopes, we use fluxes J_i for each pitch angle interval i . These interval fluxes J_i are given by Eq. 2 as weighted telescope fluxes with the circumferences (i.e., $2\pi \cdot \sin(\alpha)$; the 2π terms cancel in the ratio) at the end points of the interval i . These circumferences are directly proportional to the solid angle contributions of the telescope fluxes at the end points.

If there are any pairs of telescopes that have their folded pitch angles closer than 5 degrees from each other, we replace the fluxes of these two telescopes with the mean flux of the two. This allows the integration over longer intervals to be weighted by the fluxes measured by several telescopes. The differential fluxes for the end points of 0 and $\pi/2$ are set to be the same as differential fluxes of the telescopes with lowest and highest folded pitch angles, respectively.

3 Electron fluxes at geostationary orbit in 30–200 keV energy range

The GOES-13 MAGED data for a five year period between 1 January 2011 and 31 December 2015 were analyzed in three lower energy channels using 5-minute averages of electron flight-direction integrated fluxes determined with the method described in the previous section. The three lower energy channels centered on 40, 75, and 150 keV provided continuous coverage in the energy range from 30 to 200 keV. The MAGED data as 5-minute average fluxes are at least two orders of magnitude above the single count flux levels throughout the five year period. In the following we describe our main results with this five-year data set.

We have organized the MAGED fluxes by the coincident solar wind and interplanetary magnetic field (IMF) parameters, including solar wind pressure, density, speed, and temperature and IMF components as provided by the OMNIWeb service of the Space Physics Data Facility at the Goddard Space Flight Center (<http://omniweb.gsfc.nasa.gov/>), provided as propagated values at the nose of the magnetopause).

Figure 2 shows median electron fluxes as functions of MLT and the IMF components B_X (panels a–c), B_Y (d–f), and B_Z (g–i). The differential electron fluxes for energy 40 keV are about an order of magnitude higher than those of energy 150 keV with fluxes of energy 75 keV in between. Overall the data show quite similar features for all three energies while the average flux levels are different. The B_X values are mostly between -20 and 22 nT whereas B_Y and B_Z reach absolute values up to 35 nT (however, the plots are limited to a range between -30 and 30 nT to show the main features). The fluxes in each bin show no sharp changes near the 0 nT lines in all the panels where the number of data-points per bin is the highest. The variability of the median bin values clearly increase with the distance from the 0 nT lines as the number of datapoints per bin decreases.

In all the panels the average fluxes are higher in the post-midnight and dawn MLT sectors. The highest flux values are nearly symmetrical with respect the $B_X = 0$ and $B_Y = 0$ lines above 5 nT and below -5 nT in these sectors. With B_Z the high fluxes are especially concentrated in a large area in the night–dawn sector with B_Z values less than -5 nT. In B_X panels for energies 40 and 75 keV (panels a and b) an asymmetric flux intensification is seen at the 0 to 4 MLT sector and $B_X < -10$ nT, though the feature may not be statistically significant. In the afternoon and dusk MLT sectors there are no significant changes in the average fluxes as functions of IMF component values.

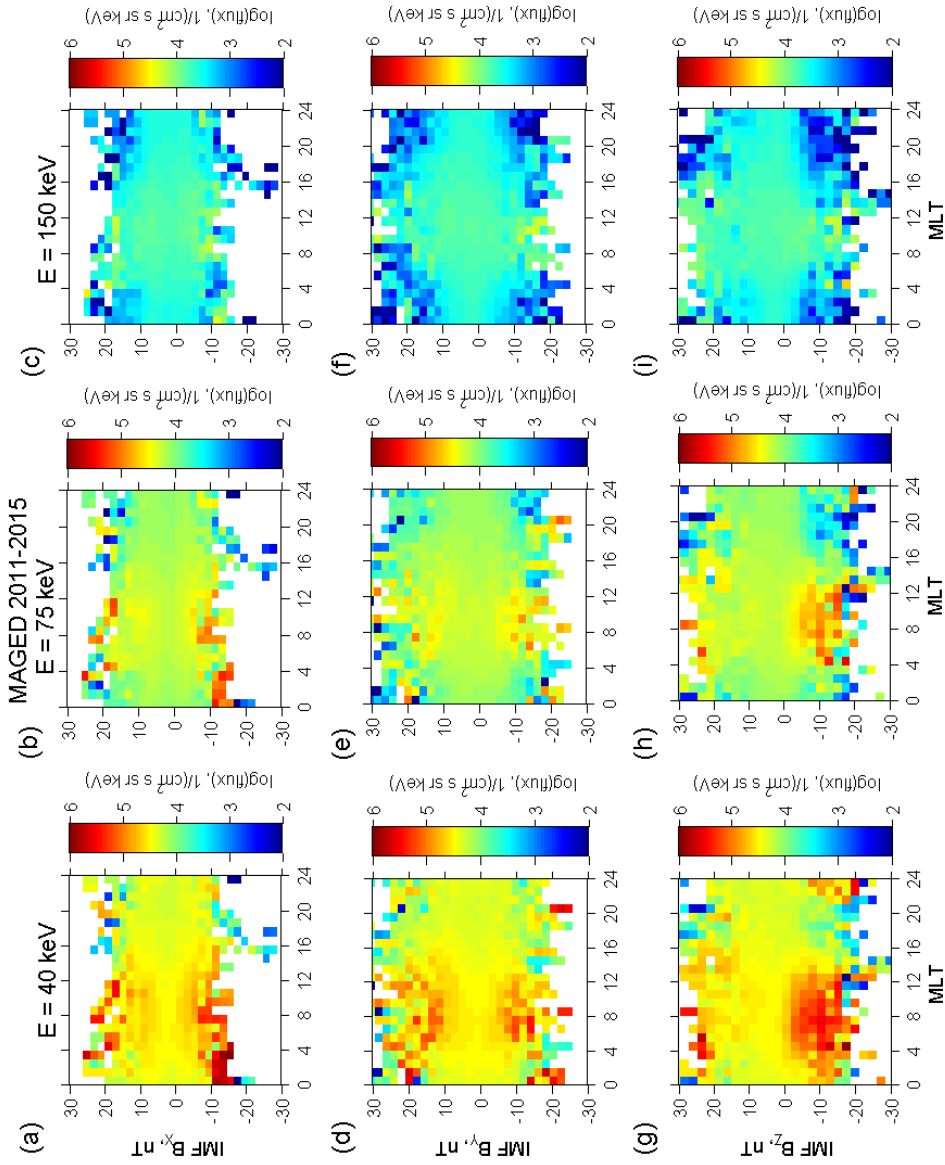


Figure 2. MAGED fluxes of energies 40, 75, and 150 keV organized with IMF components B_x , B_y , and B_z in top (a-c), middle (d-f), and bottom panels (g-i), respectively. Bin values are medians of the datapoints.

240 The solar wind parameters speed V_{SW} , density n_{SW} , pressure p_{SW} , and temperature
241 T_{SW} are used to organize the MAGED fluxes in Figure 3. The organization of MAGED
242 fluxes by the solar wind speed (panels a–c) shows nearly monotonic increases in the elec-
243 tron fluxes with increasing speed from about 250 to 800 km/s for each of the three ener-
244 gies and each MLT hour; the highest median fluxes are found in the range of 2 to 10 MLT
245 with solar wind speed above 700 km/s. Additionally, a sinusoidal shape in the logarithmic
246 fluxes can be seen with 24 MLT hours corresponding to 2π of a full sine period. There is
247 a notable shift in the phase of the sinusoidal behavior with the electron energy, with the
248 flux maximum of $V_{SW} = 400$ km/s at around 5, 7, and 9 MLT for energies 40, 75, and
249 150 keV, respectively.

250 There is considerable similarity between solar wind speed (panels a–c) and the solar
251 wind temperature (j–l): both have clear trends towards higher fluxes with higher parameter
252 values nearly in all MLTs. Solar wind density (panels d–f) and pressure (g–i) show that
253 higher density or pressure have a slight tendency to correspond to higher median fluxes in
254 the dawn sector. However, this is not the case in other MLT sectors. For example, the 12
255 to 17 MLT sector shows almost no discernible features in the electron fluxes as organized
256 with the solar wind density or pressure in all three energies (except at the highest density
257 or pressure values where the number of datapoints per bin is very low). While there are
258 distinct low flux features around density of 30 cm^{-3} and in pressure 10–20 nPa in the pre-
259 midnight sector, they are not statistically very significant due to the relatively low number
260 of datapoints per bin at those parameter values.

261 **4 Empirical model for electron fluxes at geostationary orbit for energies 40, 75, and** 262 **150 keV**

263 Based on five years of 2011–2015 of GOES-13 MAGED data, we have developed an
264 empirical model for electron fluxes at the geostationary orbit for energies 40 keV, 75 keV,
265 and 150 keV. The main aspects of the construction of the model are explained in the fol-
266 lowing.

267 The electron fluxes used were 5-minute averaged flight-direction integrated MAGED
268 data from the GOES-13 satellite. The coincident solar wind and IMF parameters (pro-
269 vided by the OMNIWeb service of the Space Physics Data Facility) were studied to deter-
270 mine their correlation with the electron fluxes measured by GOES-13. The requirement of
271 coincident solar wind and IMF data reduced the number of MAGED 5-minute data points

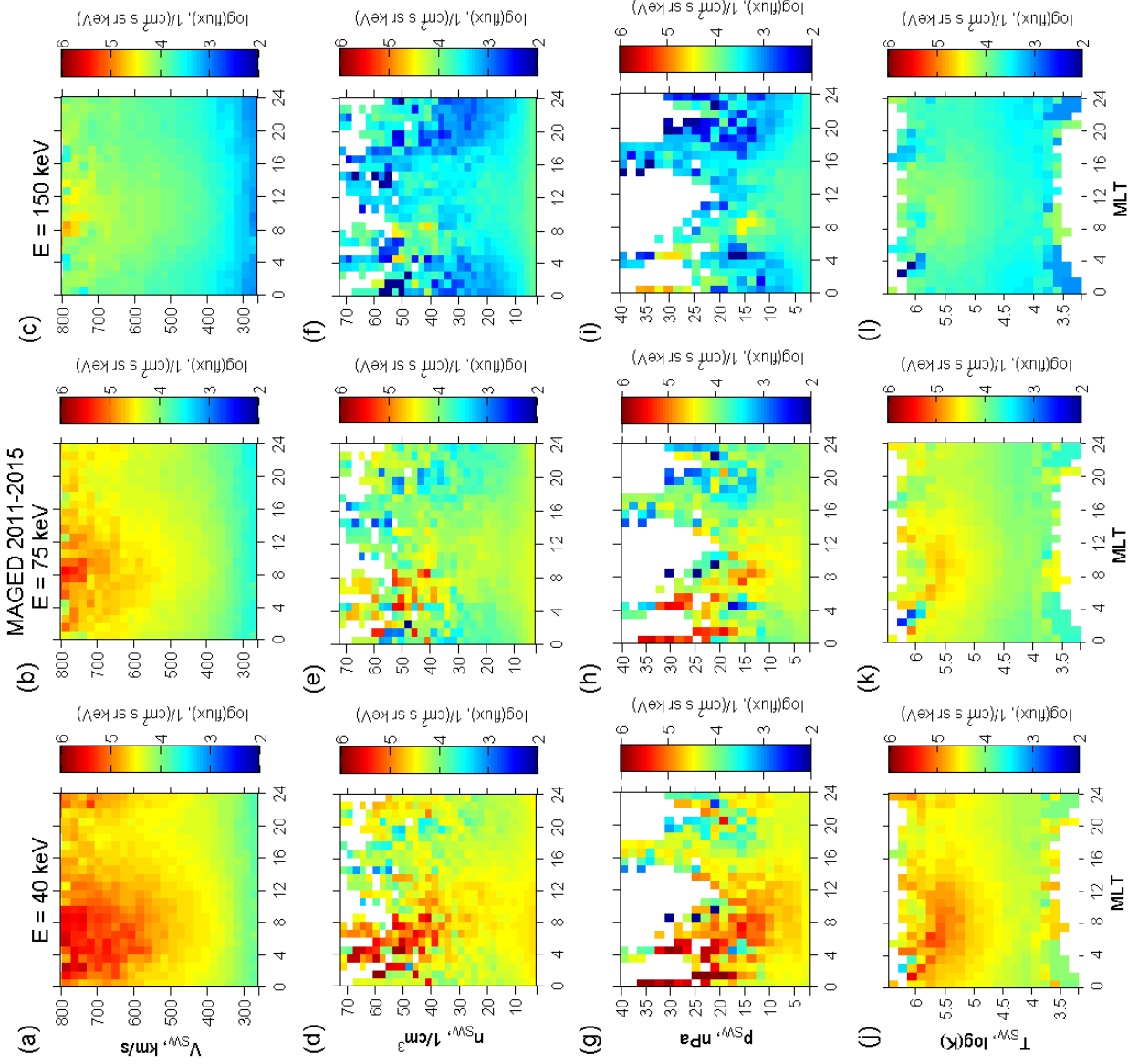


Figure 3. MAGED fluxes of energies 40, 75, and 150 keV organized with solar wind parameters speed V_{SW} , density n_{SW} , and pressure p_{SW} in top (a–c), middle (d–f), and bottom panels (g–i), respectively. Bin values are medians of the datapoints.

272 that could be used in years 2011–2015 from 520 000 to 464 000. This was due to miss-
273 ing ACE solar wind and/or IMF data. There was a small, statistically insignificant number
274 of datapoints (123) with V_{SW} higher than 800 km/s mostly in the dawn sector that were
275 excluded from the data set. A continuous solar wind speed coverage in MLT hours was
276 found to extend from the lowest data set values of about 250 to about 800 km/s with V_{SW}
277 bin width of about 30 km/s (See Figure 3 panels a–c).

278 Plots with the MAGED electron fluxes organized with solar wind and IMF param-
279 eters and MLT (e.g., Figures 2 and 3) were used to visually examine potential ways to con-
280 struct the model function (i.e. looking for features in the plots that could be modeled with
281 simple functional forms). In addition, linear correlation coefficients (CC) were calculated
282 between solar wind speed, pressure, density and temperature as well as with IMF com-
283 ponents for the MAGED fluxes for energies 40, 75, and 150 keV. The highest correlation
284 coefficients by far are with the solar wind speed: 0.3059, 0.3492, and 0.4191 for energies
285 40, 75, and 150 keV, respectively. The MAGED fluxes showed sinusoidal-like behavior
286 with MLT when organized by V_{SW} as described in the previous section. Other param-
287 eters show significantly lower correlations with MAGED data. The parameters that have
288 absolute CC larger than 0.1 with the MAGED data are IMF $|B|$ in energies 40 and 75 keV
289 (0.136 and 0.11, respectively), IMF B_Z in energies 40 and 75 keV (-0.158, - 0.115), n_{SW}
290 in energy 150 keV (-0.163), p_{SW} in energies 40 and 75 keV (0.118, 0.104), and T_{SW} in all
291 energies (0.188, 0.203, 0.197).

292 While solar wind speed seemed a promising base for the empirical model, more pa-
293 rameters were needed to create a viable model. The solar wind temperature has the sec-
294 ond highest absolute CC with MAGED data; however, it has a strong correlation with
295 the solar wind speed (CC=0.628) and that meant that it was not likely to be a suitable
296 parameter to use in addition to the solar wind speed. Three test functions were created
297 of the form $a \cdot 10^{b \cdot V_{SW} \cdot \sin(\frac{\pi}{12} \cdot MLT + c) + d}$ for three lower MAGED energies. The test func-
298 tion residuals of the MAGED data were used to search for additional model parameters.
299 Other solar wind and IMF parameters were studied for viability by calculating their CC
300 and plotting the MAGED data or the test function residuals organized by that parameter.
301 Negative IMF B_Z component values in the post-midnight and dawn sectors correlated with
302 increased electron fluxes. This is seen as a wide peak centered around -10 nT in Figure 2.
303 Both solar wind density and pressure plots showed some enhancements of electron fluxes
304 (see Figure 3), but the residuals from the V_{SW} test functions showed only weak enhance-

305 ments, if any, as the density and pressure did not provide meaningful additions to the flux
 306 patterns in the test functions based on organization by the solar wind speed. Tests con-
 307 ducted by building model functions based on solar wind density or pressure combined
 308 with IMF B_Z component peak failed as the resulting CC between MAGED data and the
 309 values from such test functions were significantly lower than with the solar wind speed
 310 test functions.

311 The best combination for model functions as per CC was found by combining solar
 312 wind speed and IMF B_Z features. The empirical model functions were built based on the
 313 sinusoidal shape in the electron flux responses to the solar wind speed and added with a
 314 flux peak near dawn sector MLT for negative B_Z . The fitting routines used were iterative
 315 least squares algorithms.

316 The final functional form for the empirical model was found as presented below.
 317 The empirical model function provides flight-direction integrated differential electron
 318 fluxes f_{EMP} (in units of $1/(\text{cm}^2 \text{ s sr keV})$) at geostationary orbit as

$$319 \quad f_{EMP} = a1 \cdot 10^{V_{SW}} \cdot (a2 \cdot \text{sMLT} + a3 \cdot \text{cMLT} + a4) \\
 320 \quad + b1 \cdot \exp \left[-\frac{12 - |\text{MLT} - b2| - 12|}{b3} - \left(\frac{B_Z + 11}{8} \right)^3 \right] + c1, \quad (3)$$

322 where

$$323 \quad \text{sMLT} = \sin \left(\frac{\pi}{12} \cdot \text{MLT} \right), \quad (4)$$

$$324 \quad \text{cMLT} = \cos \left(\frac{\pi}{12} \cdot \text{MLT} \right). \quad (5)$$

326 The model inputs are the MLT (corresponds to a set time and location on a geosta-
 327 tionary orbit), the IMF B_Z and the solar wind speed V_{SW} . MLT is given in hours; B_Z is
 328 in units of nT, and V_{SW} in km/s. Term $12 - |\text{MLT} - b2| - 12|$ is the shortest time differ-
 329 ence between MLT and parameter $b2$ (0 and 24 hours in MLT are the same).

330 A further inspection revealed that a time delay of 1.5 hours for the solar wind speed
 331 and B_Z significantly improved the empirical model. Time delays between 0 and 3 hours
 332 were fitted and tested separately for input parameters B_Z and V_{SW} ; the highest CC with
 333 MAGED data were clearly with a time delay of 1.5 hour for B_Z . The time delays for V_{SW}
 334 with the highest correlations were found between 1 and 2 hours, each energy having dif-
 335 ferent trend as a function of time delay. With the 1.5-hour delay for both of these param-
 336 eters, CC between the electron fluxes of the empirical model and MAGED data are 0.567,

0.504, 0.486 for the MAGED energies of 40, 75, and 150 keV, respectively, for the time period 2011-2015. The prediction efficiencies are 0.321, 0.206, and 0.229 for the energies 40, 75, and 150 keV, respectively, showing that the model's performance is superior to averages of the MAGED data. Without any time delay for the solar wind speed and IMF the CC would be lower by 0.076 for the 40 keV energy, by 0.056 for 75 keV, and by 0.018 for 150 keV. Therefore the IMF and solar wind speed values used are delayed by 1.5 hours in the final model; i.e. $V_{SW} = V_{SW}(t + 1.5h)$, $B_Z = B_Z(t + 1.5h)$, $MLT = MLT(t)$, and $f_{EMP} = f_{EMP}(t)$, where t is time.

A realization that helped in reducing the number of energy dependent parameters to eight in the model (see Table 1) was that three originally energy-channel-dependent parameters could be replaced with constants in the exponent function of the B_Z term resulting in term $((B_Z + 11)/8)^3$; these values (11, 8, and 3) determine the location (as in -11 nT), width scale (8 nT), and shape (with the exponent of 3) of the flux peak for negative B_Z values. The final model coefficients for three energies are provided in Table 1.

Table 1. Coefficients of the empirical model for electron fluxes at the geostationary orbit.

Parameter	40 keV	75 keV	150 keV
a1	8 500	76 000	15 000
a2	3.3×10^{-4}	4.5×10^{-5}	2.6×10^{-5}
a3	1.7×10^{-4}	0	-5×10^{-5}
a4	1.8×10^{-3}	5×10^{-4}	5×10^{-4}
b1	299 000	97 700	11 100
b2	6.4	7.8	8.4
b3	4.9	4.6	2.9
c1	-19 300	-98 600	-19 000

Table 2 presents CC for each 6-hour MLT sector in comparison to the overall CC. For the 0 to 6 MLT sector, CC between MAGED electron fluxes and the model results are significantly higher than the overall values. The evening to midnight sector (18–24) also has somewhat higher CC, while the lowest CC are in the pre-noon sector 6–12. That the nightside MLT sectors and especially the post-midnight sector have higher CC is ex-

360 **Table 2.** Linear correlation coefficients between the empirical model and MLT quadrants and all data for
 361 energies 40, 75, and 150 keV.

MLT sector	40 keV	75 keV	150 keV
0–6	0.603	0.556	0.527
6–12	0.520	0.430	0.444
12–18	0.561	0.504	0.475
18–24	0.583	0.516	0.489
all	0.567	0.504	0.486

367 plainable with the low energy electron source from the magnetospheric tail driven by solar
 368 wind affecting these sectors most directly via enhanced convection and substorm injections
 369 (e.g., *Birn et al.* [1998]; *Ganushkina et al.* [2013]).

362 The empirical model was tested with the GOES-13 MAGED data of the first four
 363 months of year 2016 which was not included in model development. The test period had
 364 34 542 MAGED data points as 5-minute averages, and 30 942 data points that coincided
 365 with available solar wind and IMF measurements. For this period, the correlation coeffi-
 366 cients between empirical model results and the MAGED electron fluxes are 0.548, 0.489,
 367 and 0.499 and prediction efficiencies (PE) 0.294, 0.219, and 0.2027 for energies 40, 75,
 368 and 150 keV, respectively. These CC and PE values vary a little from those obtained for
 369 the five year period that the model construction was based on; the differences is CC are
 370 only 0.02 or less.

371 Figure 4 shows the MAGED electron flux values against the electron fluxes given
 372 by the empirical model for 40 (panel a), 75 (b), and 150 keV (c) for the five year period
 373 of data used in the model construction and similar plots for the four months of the test
 374 period (panels d, e, and f). There is a noticeable feature, especially in the plots of en-
 375 ergies 75 and 150 keV, of an overestimation of low MAGED flux values by the model.
 376 The modeled fluxes are 10^4 – 10^6 $1/(\text{cm}^2 \text{ s sr keV})$ for 75 keV and between 10^3 and 10^4
 377 $1/(\text{cm}^2 \text{ s sr keV})$ for 150 keV when the corresponding observed fluxes were less than 10^3
 378 and $5 \cdot 10^2$ $1/(\text{cm}^2 \text{ s sr keV})$, respectively. For the highest values of the observed fluxes the

379 model underestimates the measured electron fluxes: this is most pronounced for 75 keV
380 energy around $5 \cdot 10^5$ $1/(\text{cm}^2 \text{ s keV})$ and for 150 keV energy above $5 \cdot 10^4$ $1/(\text{cm}^2 \text{ s keV})$
381 in MAGED flux values. The test period results from early 2016 (panels d–f) exhibit very
382 similar features.

383 The empirical model mostly failed to capture the low flux tails of MAGED data as
384 seen in Figure 4. To better understand possible underlying reasons for the low flux tails,
385 we present Figure 5 that organizes the low fluxes with MLT and the declination of Sun.
386 The declination of the Sun (or subsolar latitude) parametrizes Earth’s seasonally varying
387 tilt with respect to the Sun. Together with MLT, the declination of the Sun organized well
388 the low flux data. The upper cutoff limits of the fluxes shown ($2 \cdot 10^3$, $5 \cdot 10^2$, and 50
389 $1/(\text{cm}^2 \text{ s sr keV})$ for 40, 75, and 150 keV, respectively) were set so that the number of data
390 points below the limit were close to each other for each of the three energies (between
391 3229 and 3353 data points).

392 Figure 5 shows that the lowest fluxes are concentrated to the nightside between 18
393 and 4 MLT. The frequency of low fluxes peaks sharply at the highest declination values
394 (> 21 degrees, i.e. June and most of July), with highest numbers of data points right be-
395 fore midnight (maximum number of datapoints per bin were between 155 and 180 for the
396 three energies). There seems to be a trend for these low fluxes to occur more frequently
397 with positive declination than with negative.

398 Additional tests showed some improvement in CC between the MAGED data and
399 the empirical model when criteria for omission of high-declination datapoints in the night-
400 sector was used in order to reduce the influence of the low flux tails. However, any tried
401 criteria, that excluded most of the low flux datapoints defined by the low flux limits given
402 above, removed also more than $6 \cdot 10^4$ other datapoints (about 14 percent of all data).

403 Figure 6 shows the MAGED data (upper row of panels) organized by IMF B_Z and
404 MLT and compared with the empirical model results (lower row of panels) for the same
405 time period from January 2011 to December 2015. Figure 7 presents similar comparison
406 but with the electron fluxes organized solar wind speed V_{SW} and MLT. These parame-
407 ters, IMF B_Z , V_{SW} , and MLT, are all the input parameters used in the developed empirical
408 model. The bin size used in the panels for modeled fluxes is smaller to demonstrate the
409 patterns even with small number of data points. The modeled fluxes successfully replicate

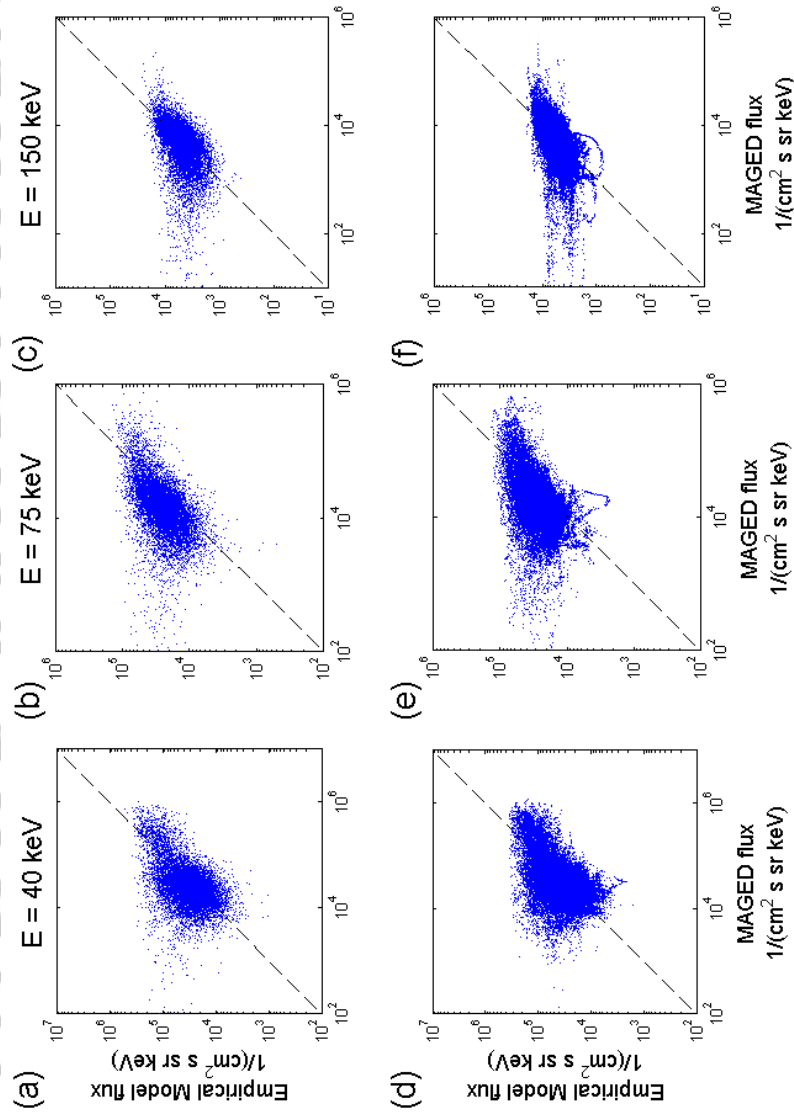


Figure 4. MAGED electron flux versus the electron fluxes given by the empirical model for (a) 40, (b) 75, (c) 150 keV for period 2011–2015 with every 50th data point shown. The MAGED electron flux vs the empirical model results for a four month test period January–April 2016 are shown below (d–f) with all data points shown.

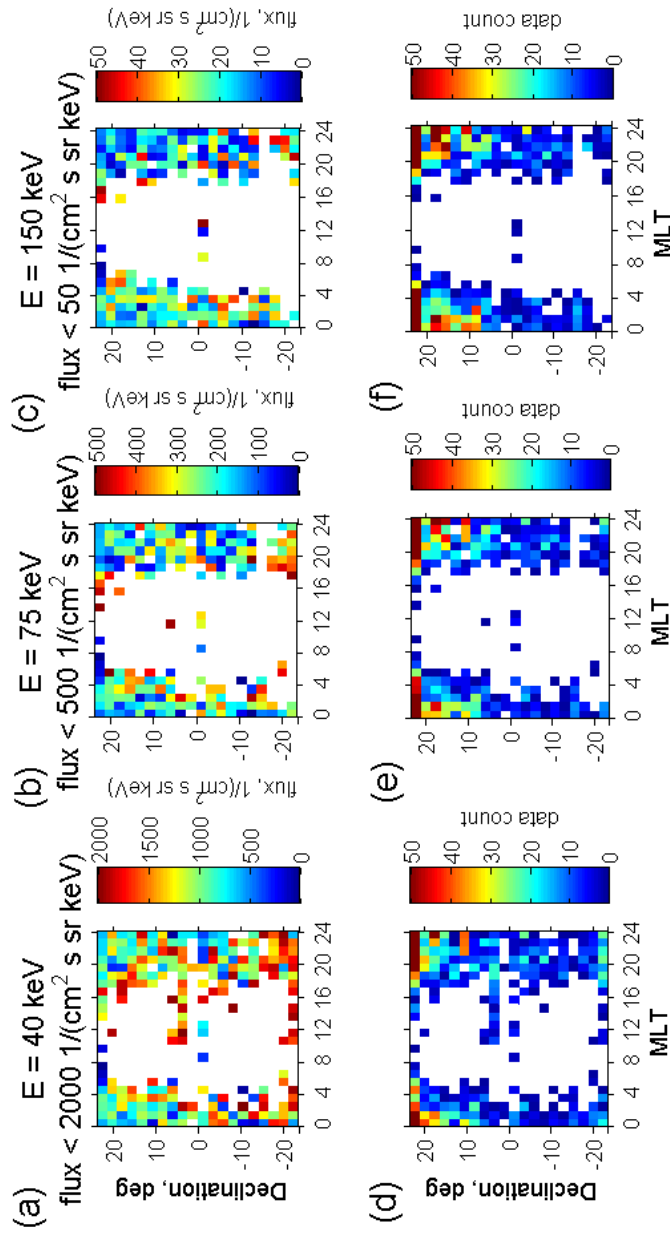


Figure 5. Low values of MAGED electron fluxes are shown against MLT and the declination of the Sun as medians (panels a–c) and as the number of data points per bin (d–f) for the 2011–2015 period. The upper limits of the flux values for the accepted data points were $2 \cdot 10^3$, $5 \cdot 10^2$, and $50 \text{ 1/(cm}^2 \text{ s sr keV)}$ for 40, 75, and 150 keV, respectively. White areas are bins without any assigned data points.

410 the main patterns of the electron flux data. The bin values are averages of the fluxes as
411 that correspond well with the root mean square fitting done for the model.

412 **5 Discussion and Conclusions**

413 The geostationary satellite GOES-13 has provided a significant data set of keV range
414 electrons with its MAGED instrument. We have analyzed five full years of that data and
415 based on it developed an empirical model for 40, 75, and 150 keV electrons at any geosta-
416 tionary orbit. The developed model uses solar wind and IMF parameters as input, namely
417 solar wind speed and the Z component of the IMF. The model reproduces well the ob-
418 served electron fluxes.

419 The linear correlation coefficients between the MAGED electron fluxes at geosyn-
420 chronous orbit and solar wind speed are (with no time delay) are from 0.30 to 0.42 (mod-
421 erate correlations). The correlation coefficients between MAGED fluxes and the final,
422 time-delayed empirical model are between 0.49 and 0.57 (stronger correlations). These
423 correlations indicate that the solar wind speed has an effect on the electron fluxes, but it is
424 a connection that takes place through a number of magnetospheric processes.

425 Employing geomagnetic indices (with significantly better correlation coefficients for
426 the MAGED data than solar wind or IMF parameters) would likely have made the empir-
427 ical model more accurate in the fluxes overall. However, our purpose in this study was to
428 quantify and model the effect that solar wind and IMF conditions have on electron fluxes
429 at geosynchronous orbit. Furthermore, an empirical model using solar wind and IMF pa-
430 rameters suits much better for forecasting purposes and is not dependent on anything but
431 observations taken in the upstream solar wind. This together with the time delay of 1.5
432 hours for the input parameters IMF B_Z and solar wind speed makes the model usable for
433 forecasting purposes.

434 A feasible method for improving the presented empirical model could be to use time
435 averaging of the model parameters. This would mean searching for optimal delayed time
436 ranges for the input parameters V_{SW} and IMF B_Z . Likely this would have to be done by
437 MLT sectors as the delays are expected to vary significantly with the magnetospheric loca-
438 tion (cf. *Hartley et al.* [2014]). The method was recently applied by *Dubyagin et al.* [2016]
439 for a very successful prediction model of the parameters of the magnetospheric tail.

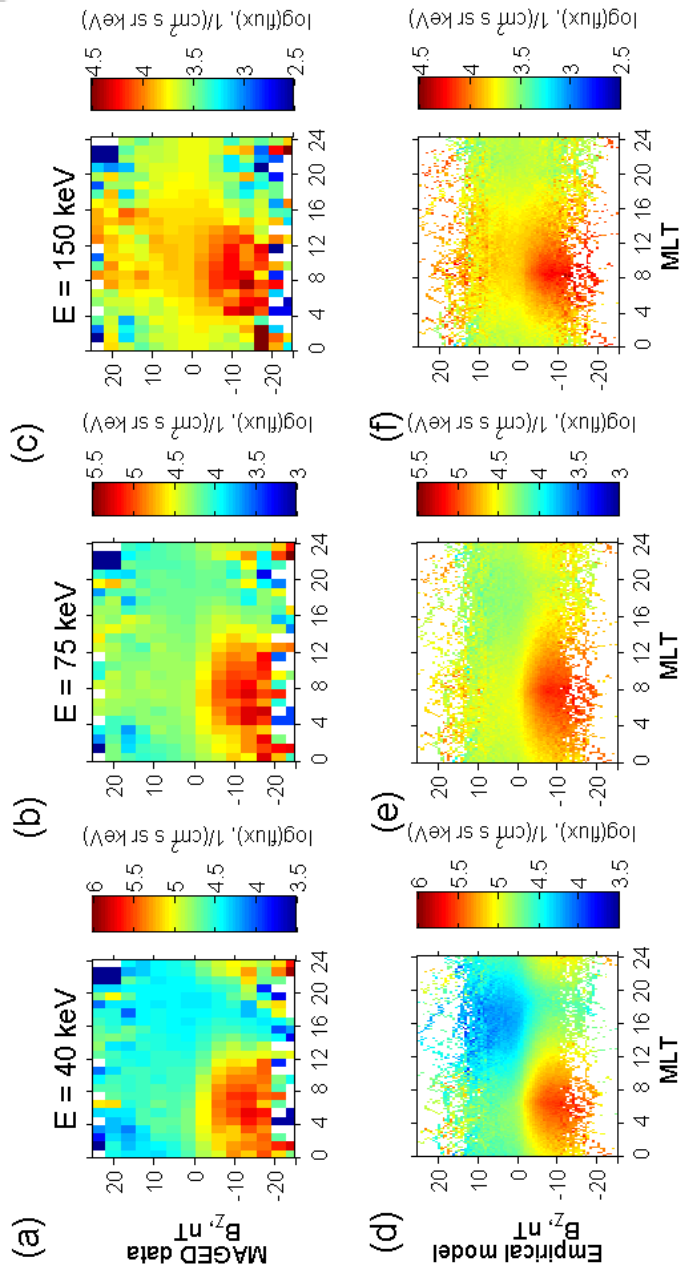


Figure 6. MAGED data (a, b, c) as dependent on IMF B_Z and MLT compared with the empirical model results (d, e, f) for the same time period from January 2011 to March 2015. Bin values are averages.

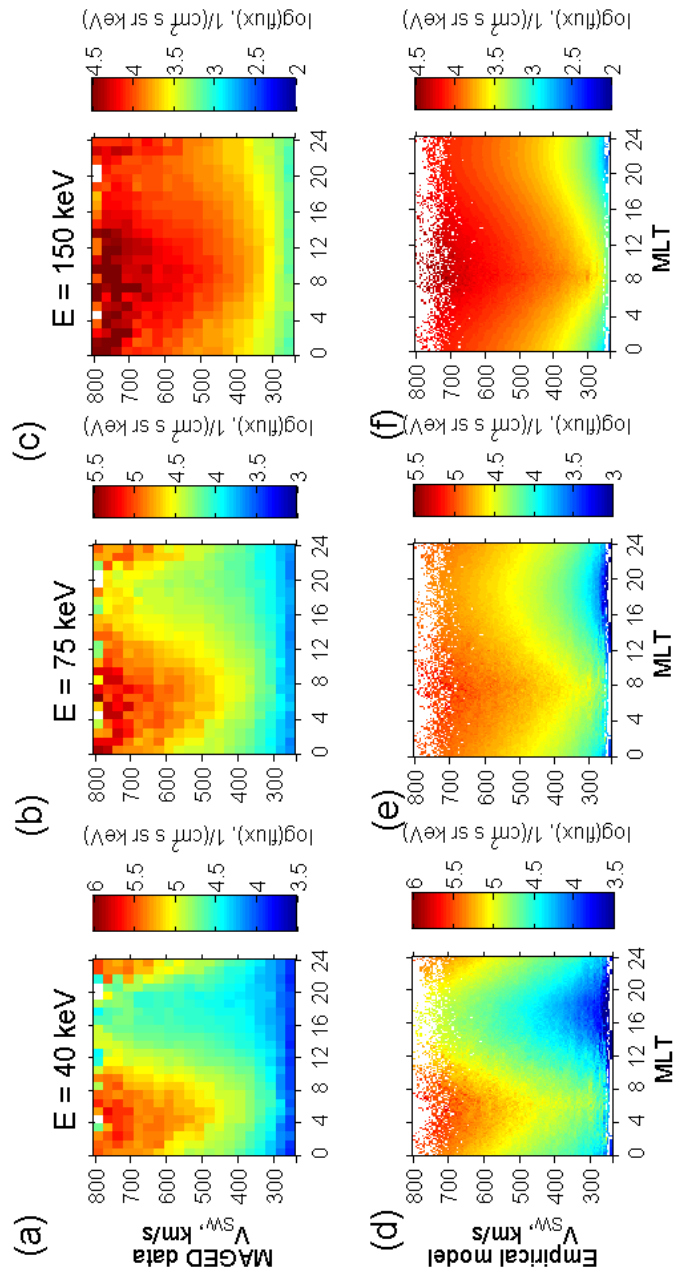


Figure 7. Similar to Figure 6 with electron fluxes dependent on solar wind speed V_{SW} and MLT.

440 Our statistical results on the electron low flux tail in the 30–150 keV energies showed
441 higher occurrence of low flux events from dusk to dawn centered on local midnight and
442 around the June solstice over the studied five years. Very low fluxes at geosynchronous
443 orbit are associated with stretched magnetic fields, as the partial ring current develops
444 during storm times (e.g. *Green et al.* [2004]), or just prior to substorm particle injections
445 (e.g. *Loto'aniu et al.* [2015]), and they can also ensue after long geomagnetically-quiet pe-
446 riods (e.g. *Jaynes et al.* [2015]). Mechanisms associated with disparate solar wind velocity
447 and IMF conditions can thus lead to very low fluxes at geosynchronous orbit, possibly
448 weakening correlations with solar wind and IMF parameters. It is interesting that the low
449 flux tails in our statistics are not symmetric with respect to June and December solstice. It
450 may be possible that the location of GOES-13 at 75W longitude and the positive magnetic
451 latitude at that position 11 degrees north [*Onsager et al.*, 2004] is behind the asymmetry.
452 Further research would be advisable on these low flux phenomena.

453 Keeping in mind the points discussed above, our conclusions are the following:

- 454 1. Solar wind speed has a moderate correlation with the geostationary keV-range
455 electron fluxes for all MLT sectors.
- 456 2. IMF B_Z has a significant influence in the 0 to 12 MLT sector where the B_Z less
457 than -5 nT leads to elevated electron fluxes in the 30–200 keV energy range.
- 458 3. Electrons with energies from 30 to 200 keV have particularly low flux periods
459 that occur mainly in the night sector and have a clear seasonal preference.
- 460 4. The constructed empirical model can have a variety of applications from fore-
461 casting electron fluxes at geostationary or geosynchronous orbits to being an input to other
462 models such as serving as low-energy boundary conditions for studying electron accelera-
463 tion to MeV energies.

464 **Acknowledgments**

465 The original data used in this study is publicly available as follows. The directional
466 differential fluxes of the MAGED telescopes and their pitch angles are provided in the
467 NOAA archival data (http://satdat.ngdc.noaa.gov/sem/goes/data/new_avg/). The solar wind
468 and interplanetary magnetic field (IMF) parameters, namely solar wind pressure, density,

469 speed, and temperature and IMF components are provided by the OMNIWeb service of
470 the Space Physics Data Facility at the Goddard Space Flight Center (<http://omniweb.gsfc.nasa.gov/>).

471 The projects leading to these results have received funding from the European Union
472 Seventh Framework Programme (FP7/2007-2013) under grant agreement No 606716 SPACES-
473 TORM and from the European Union's Horizon 2020 research and innovation program
474 under grant agreement No 637302 PROGRESS. N. Ganushkina thanks the International
475 Space Science Institute in Bern, Switzerland, for their support of the international teams
476 on "Analysis of Cluster Inner Magnetosphere Campaign data, in application of the dy-
477 namics of waves and wave-particle interaction within the outer radiation belt" and "Ring
478 current modeling: Uncommon Assumptions and Common Misconceptions". Support for
479 N. Ganushkina at the University of Michigan was provided by the NASA research grants
480 NNX14AF34G and NNX17AI48G. J. Rodriguez was supported by the National Centers
481 for Environmental Information through NA15OAR4320137.

482 **References**

- 483 Åsnes, A., J. Stadsnes, R.W. Friedel, N. Østgaard, and M. Thomsen (2005), Medium en-
484 ergy pitch angle distributions during substorm injected electron clouds, *Geophys. Res.*
485 *Lett.*, *32*, L10101, doi:10.1029/2004GL022008.
- 486 Baker, D. N., P. R. Higbie, E. W. Hones, Jr., and R. D. Belian (1978), High-resolution
487 energetic particle measurements at 6.6 RE 3. Low-energy electron anisotropies
488 and short-term substorm predictions, *J. Geophys. Res.*, *83(A10)*, 4863–4868,
489 doi:10.1029/JA083iA10p04863.
- 490 Bame, S. J., McComas, D. J., Thomsen, M. F., et al. (1993), Magnetospheric
491 Plasma Analyzer for Spacecraft with Constrained Resources, *Rev. Sci. Instr.*, *64*,
492 doi:10.1063/1.1144173.
- 493 Birn, J., Thomsen, M.F., Borovsky, J.E., Reeves, G.D., McComas, D.J., Belian, R.D., and
494 Hesse, M. (1998), Substorm electron injections: Geosynchronous observations and test
495 particle simulations, *J. Geophys. Res.*, *103(A5)*, doi:10.1029/97JA02635.
- 496 Boyd, A.J., H.E. Spence, C-L. Huang, G.D. Reeves, D.N. Baker, D.L. Turner, S.G.
497 Claudepierre, J.F. Fennell, J.B. Blake, and Y.Y. Shprits (2016), Statistical properties of
498 the radiation belt seed population, *J. Geophys. Res.*, *121*, doi:10.1002/2016JA022652.
- 499 Boyle, C., Reiff, P., and Hairston, M. (1997), Empirical polar cap potentials, *J. Geophys.*
500 *Res.*, *102(A1)*, doi:10.1029/96JA01742.

501 Brautigam, D.H., and J.M. Albert (2000), Radial diffusion analysis of outer radiation
502 belt electrons during the 9 October 1990 magnetic storm, *J. Geophys. Res.*, *105*,
503 doi:10.1029/1999JA900344.

504 Chen, M.W., M. Schulz, P.C. Anderson, et al. (2005), Storm time distributions of diffuse
505 auroral electron energy and X-ray flux: Comparison of drift-loss simulations with obser-
506 vations, *J. Geophys. Res.*, *110*, A03210, doi:10.1029/2004JA010725.

507 Chen, Y., G.D. Reeves, and R.H.W. Friedel (2007), The energization of relativistic elec-
508 trons in the outer Van Allen radiation belt, *Nature Physics*, *3*, doi:10.1038/nphys655.

509 Davis, V.A., M.J. Mandell, and M.F. Thomsen (2008), Representation of the measured
510 geosynchronous plasma environment in spacecraft charging calculations, *J. Geophys.*
511 *Res.*, *113*, doi:10.1029/2008JA013116.

512 Denton, M. H., M. F. Thomsen, V. K. Jordanova, M. G. Henderson, J. E. Borovsky,
513 J. S. Denton, D. Pitchford, and D. P. Hartley (2015), An empirical model of electron
514 and ion fluxes derived from observations at geosynchronous orbit, *Space Weather*, *13*,
515 doi:10.1002/2015SW001168.

516 Denton, M. H., and J. E. Borovsky (2008), Superposed epoch analysis of high-speed-
517 stream effects at geosynchronous orbit: Hot plasma, cold plasma, and the solar wind,
518 *J. Geophys. Res.*, *113*, A07216, doi:10.1029/2007JA012998.

519 Denton, M. H., M. F. Thomsen, H. Korth, S. Lynch, J. C. Zhang, and M. W. Liemohn
520 (2005), Bulk plasma properties at geosynchronous orbit, *J. Geophys. Res.*, *110*, A07223,
521 doi:10.1029/2004JA010861.

522 Dubyagin, S., Ganushkina, N. Yu., Sillanpää, I., A. Runov, and V. Angelopoulos
523 (2016), Solar Wind Driven Variations of Electron Plasma Sheet Densities and
524 Temperatures beyond Geostationary Orbit during Storm Times, *J. Geophys. Res.*,
525 doi:10.1002/2016JA022947.

526 Friedel, R. H. W., H. Korth, M. G. Henderson, M. E. Thomsen, J. D. Scudder (2001),
527 Plasma sheet access to the inner magnetosphere, *J. Geophys. Res.*, *106*, 5845-5858.

528 Ganushkina, N. Yu., O. A. Amariutei, D. Welling, and D. Heynderickx (2015), Now-
529 cast model for low-energy electrons in the inner magnetosphere, *Space Weather*, *13*(1),
530 doi:10.1002/2014SW001098.

531 Ganushkina, N. Yu., M. W. Liemohn, O. A. Amariutei and D. Pitchford (2014), Low-
532 energy electrons (5-50 keV) in the inner magnetosphere, *J. Geophys. Res.*, *119*,
533 doi:10.1002/2013JA019304.

534 Ganushkina, N. Yu., O. A. Amariutei, Y. Y. Shprits, and M. W. Liemohn (2013), Trans-
535 port of the plasma sheet electrons to the geostationary distances, *J. Geophys. Res.*, *118*,
536 doi:10.1029/2012JA017923.

537 Ganushkina, N. Yu., M.W. Liemohn, and T.I. Pulkkinen (2012), Storm-time ring current:
538 model-dependent results, *Ann. Geophys.*, *30*, doi:10.5194/angeo-30-177-2012.

539 Ganushkina, N. Yu., and T. I. Pulkkinen (2002), Particle tracing in the Earth's magne-
540 tosphere and the ring current formation during storm times, *Ann. Geophys.*, *30*(7),
541 doi:10.1016/S0273-1177(02)00455-6.

542 Garrett, H. B. (1981), The charging of spacecraft surfaces, *Rev. Geophys.*, *19*(4), 577,
543 doi:10.1029/RG019i004p00577.

544 Garrett, H.B., D.C. Schwank, and S.E. DeForest (1981), A statistical analysis of the low-
545 energy geosynchronous plasma environment — I. Electrons, *Planet. Space Sci.*, *29*(10),
546 1021-1044, doi:10.1016/0032-0633(81)90001-5.

547 *GOES N Series Data Book* (2010), prepared for NASA pursuant to contract NAS5-98069,
548 Revision D.

549 Green, J.C., T.G. Onsager, T.P. O'Brien, and D.N. Baker (2004), Testing loss mechanisms
550 capable of rapidly depleting relativistic electron flux in the Earth's outer radiation belt,
551 *J. Geophys. Res.*, *109*, A12211, doi:10.1029/2004JA010579.

552 Hanser, F. A. (2011), *EPS/HEPAD calibration and data handbook*, Tech. Rep. GOESN-
553 ENG-048D, Assurance Technology Corporation, Carlisle, Mass. (Available at
554 <http://www.ngdc.noaa.gov/stp/satellite/goes/documentation.html>).

555 Hartley, D. P., M. H. Denton, and J. V. Rodriguez (2014), Electron number density, tem-
556 perature, and energy density at GEO and links to the solar wind: A simple predictive
557 capability, *J. Geophys. Res.*, *119*, doi:10.1002/2014JA019779.

558 Horne, R.B., R.M. Thorne, Y.Y. Shprits et al. (2005), Wave acceleration of electrons in
559 the Van Allen radiation belts, *Nature*, *437*, 8 September 2005, doi:10.1038/nature03939.

560 Jaynes, A.N., D.N. Baker, H.J. Singer, J.V. Rodriguez, T.M. LotoÅŻaniu, A.F. Ali, S.R.
561 Elkington, X. Li, S.G. Kanekal, S.G. Claudepierre, J.F. Fennell, W.Li, R.M. Thorne,
562 C.A. Kletzing, H.E. Spence, and G.D. Reeves (2015), Source and seed populations
563 for relativistic electrons: Their roles in radiation belt changes, *J. Geophys. Res.*, *120*,
564 doi:10.1002/2015JA021234.

565 Kellerman, A. C., and Y. Y. Shprits (2012), On the influence of solar wind con-
566 ditions on the outer-electron radiation belt, *J. Geophys. Res.*, *117*, A05217,

567 doi:10.1029/2011JA017253.

568 Koons, H.C., J.E. Mazur, R.S. Selesnick, J.B. Blake, J.F. Fennell, J.L. Roeder, and
569 P.C. Anderson (1999), The Impact of the Space Environment on Space Systems,
570 *Aerospace Rep. TR-99(1670)-1*, prepared for Space and Missile Systems Center, Air
571 Force Materiel Command.

572 Korth, H., and M. F. Thomsen (2001), Plasma sheet access to geosynchronous
573 orbit: Generalization to numerical field models, *J. Geophys. Res.*, *106*(A12),
574 doi:10.1029/2000JA000373.

575 Korth, H., M. F. Thomsen, J. E. Borovsky, and D. J. McComas (1999), Plasma sheet ac-
576 cess to geosynchronous orbit, *J. Geophys. Res.*, *104*(A11), doi:10.1029/1999JA900292.

577 Lanzerotti L.J., K. LaFleur, C.G. MacLennan, and D.W. Maurer (1998), Geosynchronous
578 spacecraft charging in January 1997, *Geophys. Res. Lett.*, *25*(15), 2,967–2,970.

579 Lezniak, T. W. and J. R. Winckler (1970), Experimental Study of Magnetospheric Motions
580 and the Acceleration of Energetic Electrons during Substorms, *J. Geophys. Res.*, *75*(34),
581 doi:10.1029/JA075i034p07075.

582 Li, W., R.M. Thorne, Q. Ma, B. Ni, J. Bortnik, D.N. Baker, H.E. Spence, G.D. Reeves,
583 S.G. Kanekal, J.C. Green, C.A. Kletzing, W.S. Kurth, G.B. Hospodarsky, J.B.
584 Blake, J.F. Fennell, and S.G. Claudepierre (2014), Radiation belt electron accel-
585 eration by chorus waves during the 17 March 2013 storm, *J. Geophys. Res.*, *119*,
586 doi:10.1002/2014JA019945.

587 Li, X., D.N. Baker, M. Temerin, G. Reeves, R. Friedel, and C. Shen (2005), Energetic
588 electrons, 50 keV to 6 MeV, at geosynchronous orbit: Their responses to solar wind
589 variations, *Space Weather*, *3*, S04001, doi:10.1029/2004SW000105.

590 Loto'aniu, T.M., H.J. Singer, J.V. Rodriguez, J. Green, W. Denig, D. Biesecker, and
591 V. Angelopoulos (2015), Space weather conditions during the Galaxy 15 spacecraft
592 anomaly, *Space Weather*, *13*, doi:10.1002/2015SW001239.

593 Ma, Q., D. Mourenas, A. Artemyev, W. Li, and R.M. Thorne, Strong enhancement of
594 10–100 keV electron fluxes by combined effects of chorus waves and time domain struc-
595 tures, *Geophys. Res. Lett.*, *43*(10), doi:10.1002/2016GL069125.

596 McComas, D. J., S. J. Bame, B. L. Barraclough, J. R. Donart, R. C. Elphic, J. T. Gosling,
597 M. B. Moldwin, K. R. Moore, and M. F. Thomsen (1993), Magnetospheric plasma ana-
598 lyzer: Initial 3-spacecraft observations from geosynchronous orbit, *J. Geophys. Res.*, *98*,
599 doi:10.1029/93JA00726.

600 Onsager, T.G., A.A. Chan, Y. Fei, S.R. Elkington, J.C. Green, and H.J. Singer (2004), The
601 radial gradient of relativistic electrons at geosynchronous orbit, *J. Geophys. Res.*, *109*,
602 A05221, doi:10.1029/2003JA010368.

603 Reeves, G.D., K.L. McAdams, R.H.W. Friedel, and T.P. O'Brien (2003), Acceleration
604 and loss of relativistic electrons during geomagnetic storms, *Geophys. Res. Lett.*, *30*,
605 doi:10.1029/2002GL016513.

606 Rodriguez, J. V. (2014), *GOES 13-15 MAGE/PD pitch angles*, Algorithm Theoretical Ba-
607 sis Document, version 1.0 NOAA NESDIS NGDC, September 10, 2014 (Available at
608 <http://www.ngdc.noaa.gov/stp/satellite/goes/documentation.html>).

609 Rowland, W., and R. S. Weigel (2012), Intracalibration of particle detectors on
610 a three-axis stabilized geostationary platform, *Space Weather*, *10*, S11002,
611 doi:10.1029/2012SW000816.

612 Sicard-Piet, A., S. Bourdarie, D. Boscher, R. H. W. Friedel, M. Thomsen, T. Goka,
613 H. Matsumoto, and H. Koshiishi (2008), A new international geostationary elec-
614 tron model: IGE-2006, from 1 keV to 5.2 MeV, *Space Weather*, *6*, S07003,
615 doi:10.1029/2007SW000368.

616 Shi, Y., E. Zesta, and L. R. Lyons (2009) Features of energetic particle radial profiles in-
617 ferred from geosynchronous responses to solar wind dynamic pressure enhancements,
618 *Ann. Geophys.*, *27*, doi:10.5194/angeo-27-851-2009.

619 Shprits, Y. Y., N. P. Meredith, and R. M. Thorne (2007), Parameterization of radiation belt
620 electron loss timescales due to interactions with chorus waves, *Geophys. Res. Lett.*, *34*,
621 L11110, doi:10.1029/2006GL029050.

622 Thomsen, M. F., M. H. Denton, B. Lavraud, and M. Bodeau (2007), Statistics of plasma
623 fluxes at geosynchronous orbit over more than a full solar cycle, *Space Weather*, *5*,
624 S03004, doi:10.1029/2006SW00257.

625 Thomsen, M. F., M. G. Henderson, and V. K. Jordanova (2013), Statistical properties of the
626 surface-charging environment at geosynchronous orbit, *Space Weather*, *11*, 237–244,
627 doi:10.1002/swe.20049.

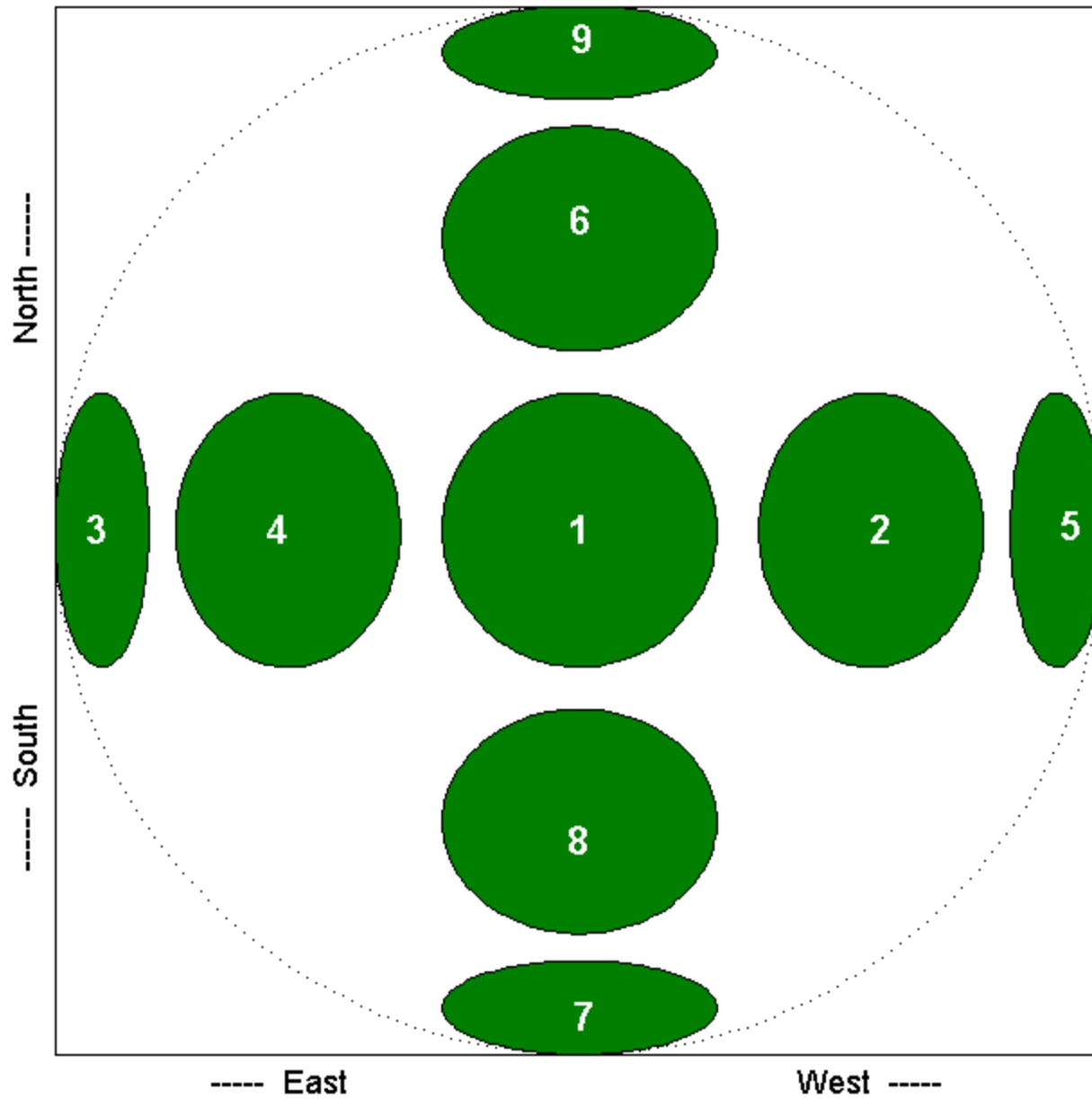
628 Tsyganenko, N. A. (1995), Modeling the Earth's magnetospheric magnetic field confined
629 within a realistic magnetopause, *J. Geophys. Res.*, *100*, doi:10.1029/94JA03193.

630 Tsyganenko, N. A., and T. Mukai (2003), Tail plasma sheet models derived from Geotail
631 particle data, *J. Geophys. Res.*, *108*(A3), 1136, doi:10.1029/2002JA009707.

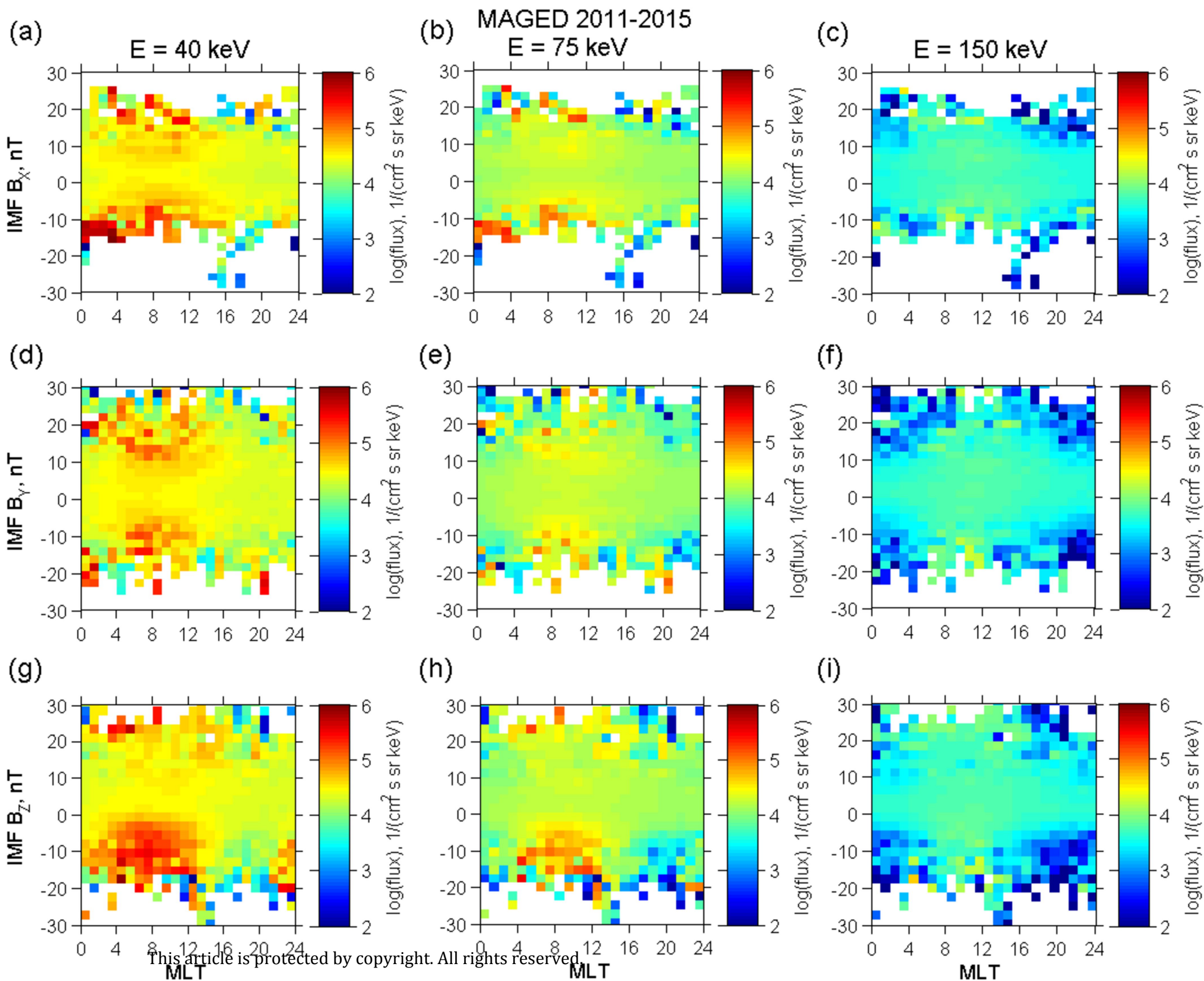
- 632 Stern, D. (1975), The Motion of a Proton in the Equatorial Magnetosphere, *J. Geophys.*
633 *Res.*, *80(4)*, doi:10.1029/JA080i004p00595.
- 634 Turner, D.L., J.F. Fennell, J.B. Blake et al. (2016), Energy limits of electron acceleration
635 in the plasma sheet during substorms: A case study with the Magnetospheric Multiscale
636 (MMS) mission, *Geophys. Res. Lett.*, *43(15)*, doi:10.1002/2016GL069691.
- 637 Turner, D.L., and X. Li (2008), Quantitative forecast of relativistic electron flux
638 at geosynchronous orbit based on low-energy electron flux, *Space Weather*, *6*,
639 doi:10.1029/2007SW000354.
- 640 Volland, H. (1973), A Semiempirical Model of Large-Scale Magnetospheric Electric
641 Fields, *J. Geophys. Res.*, *78(1)*, doi:10.1029/JA078i001p00171.

Author Manuscript

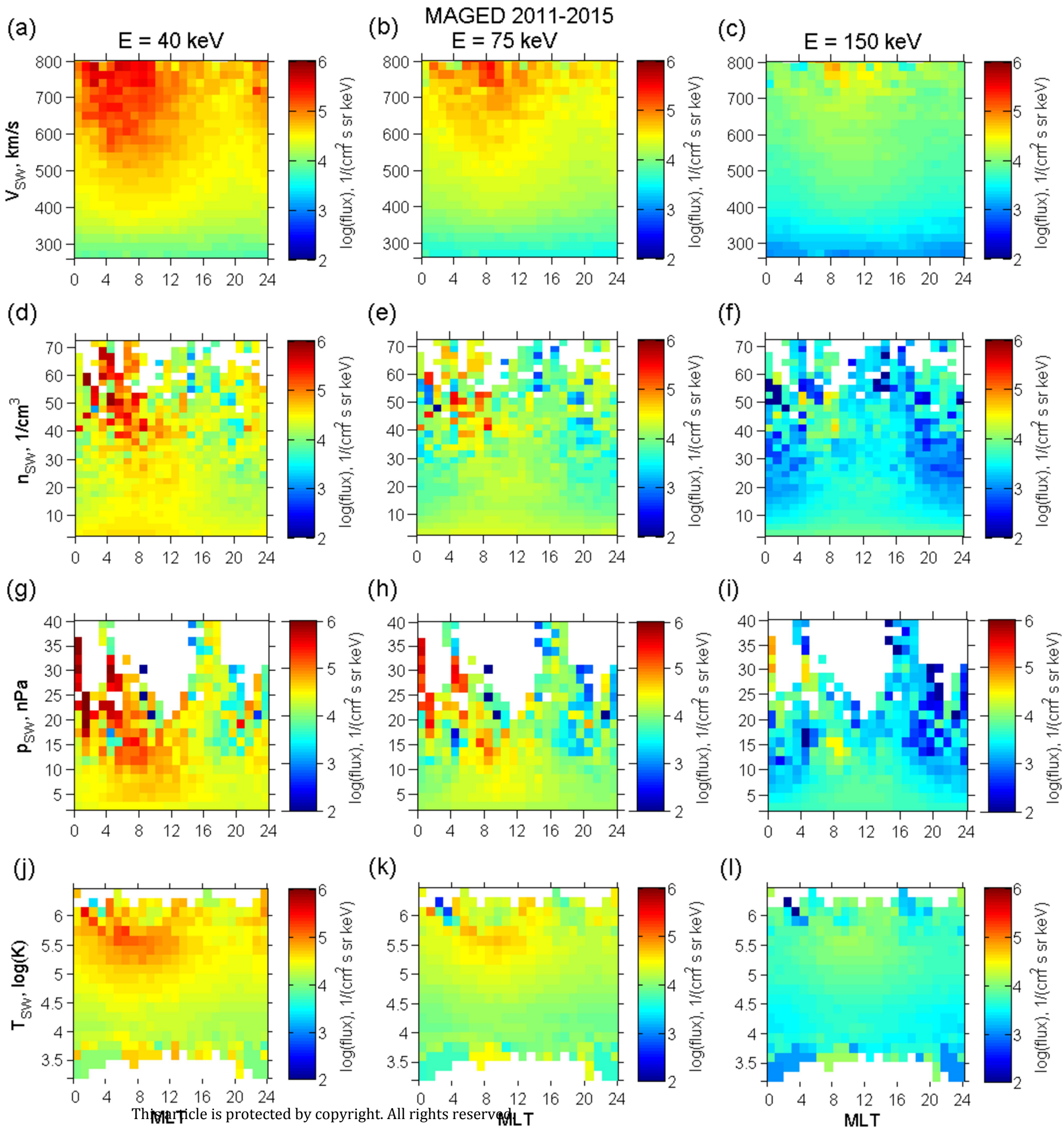
GOES-13 MAGED Field of View



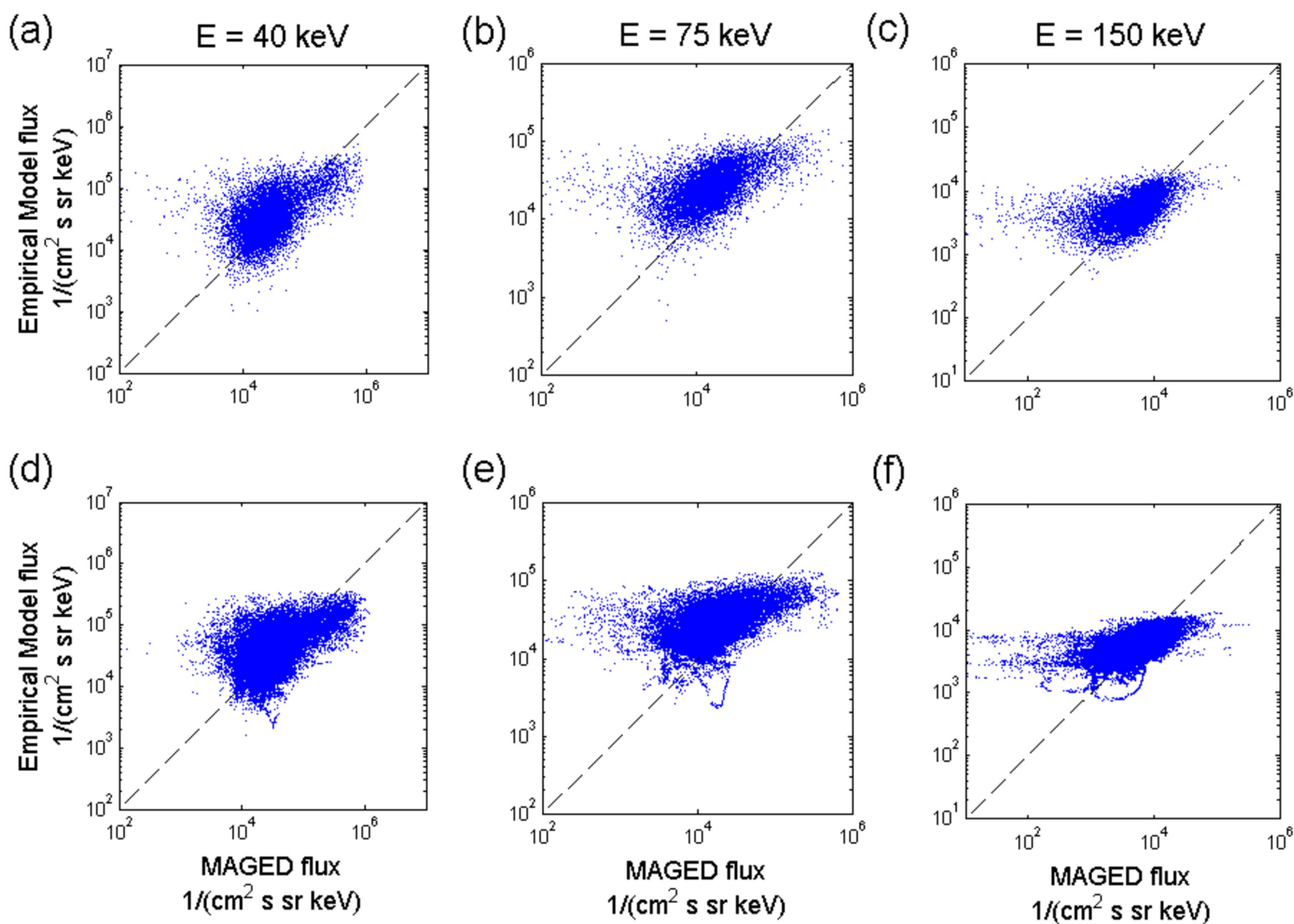
Author Manuscript



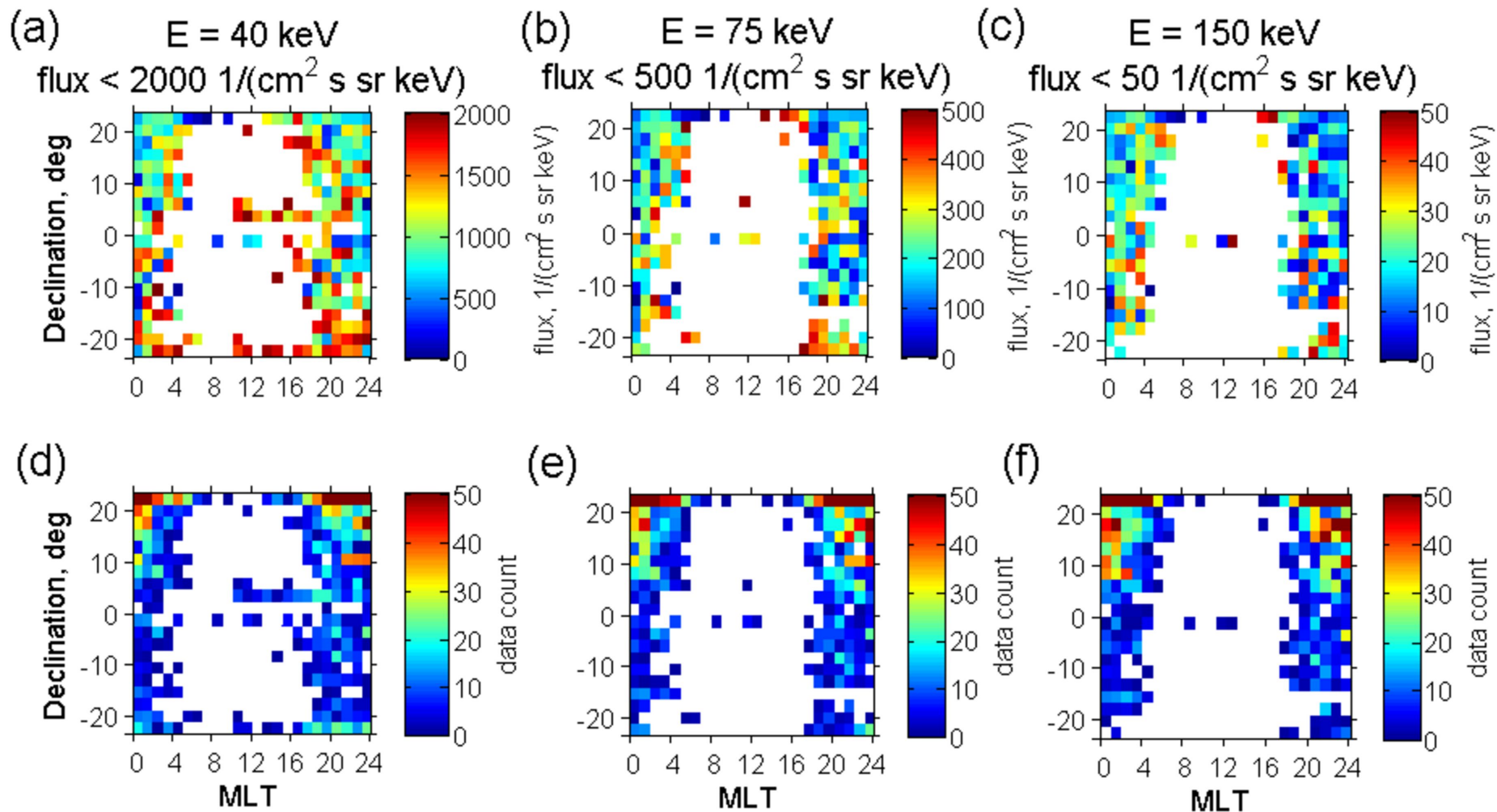
Author Manuscript



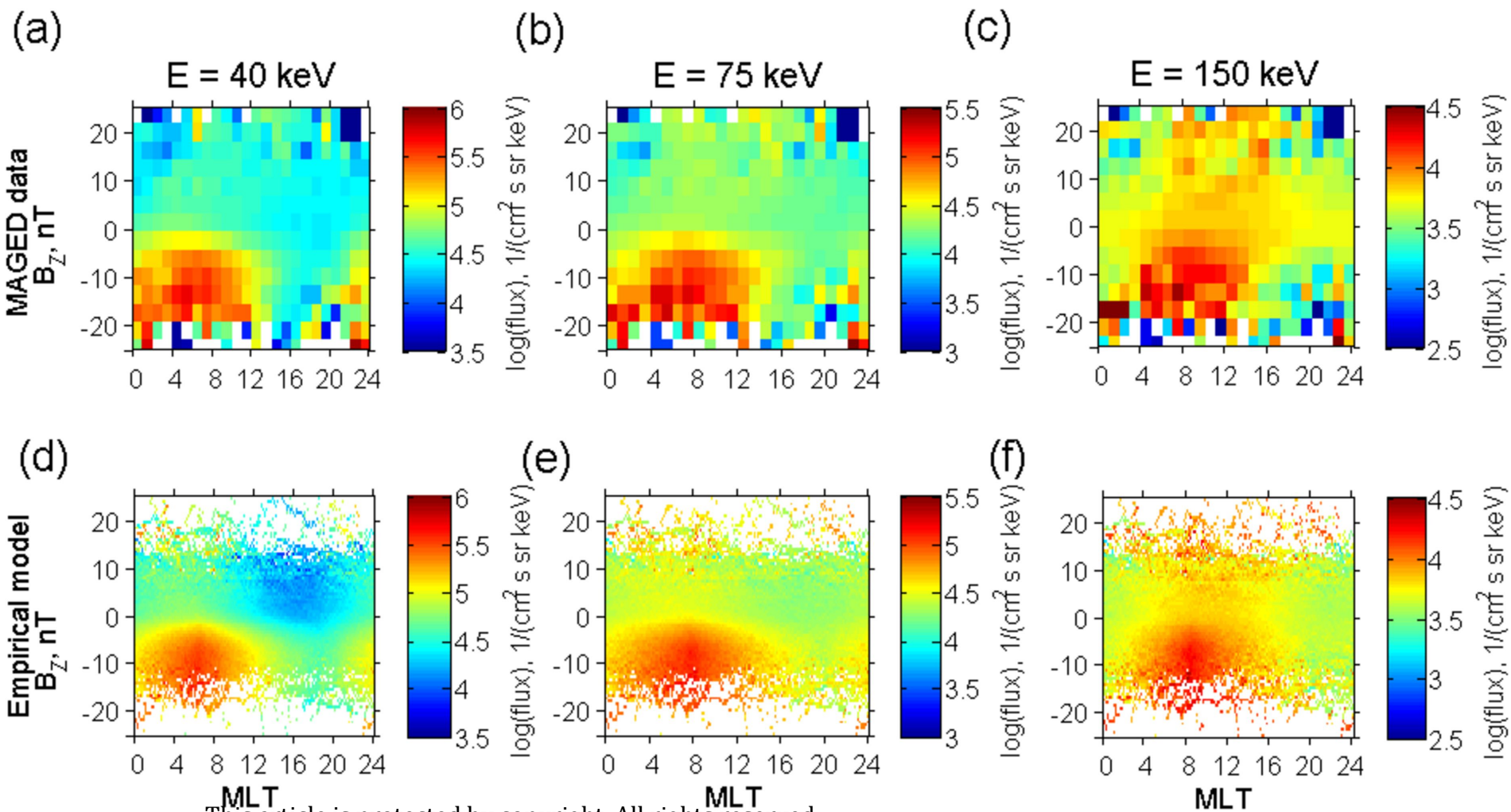
Author Manuscript



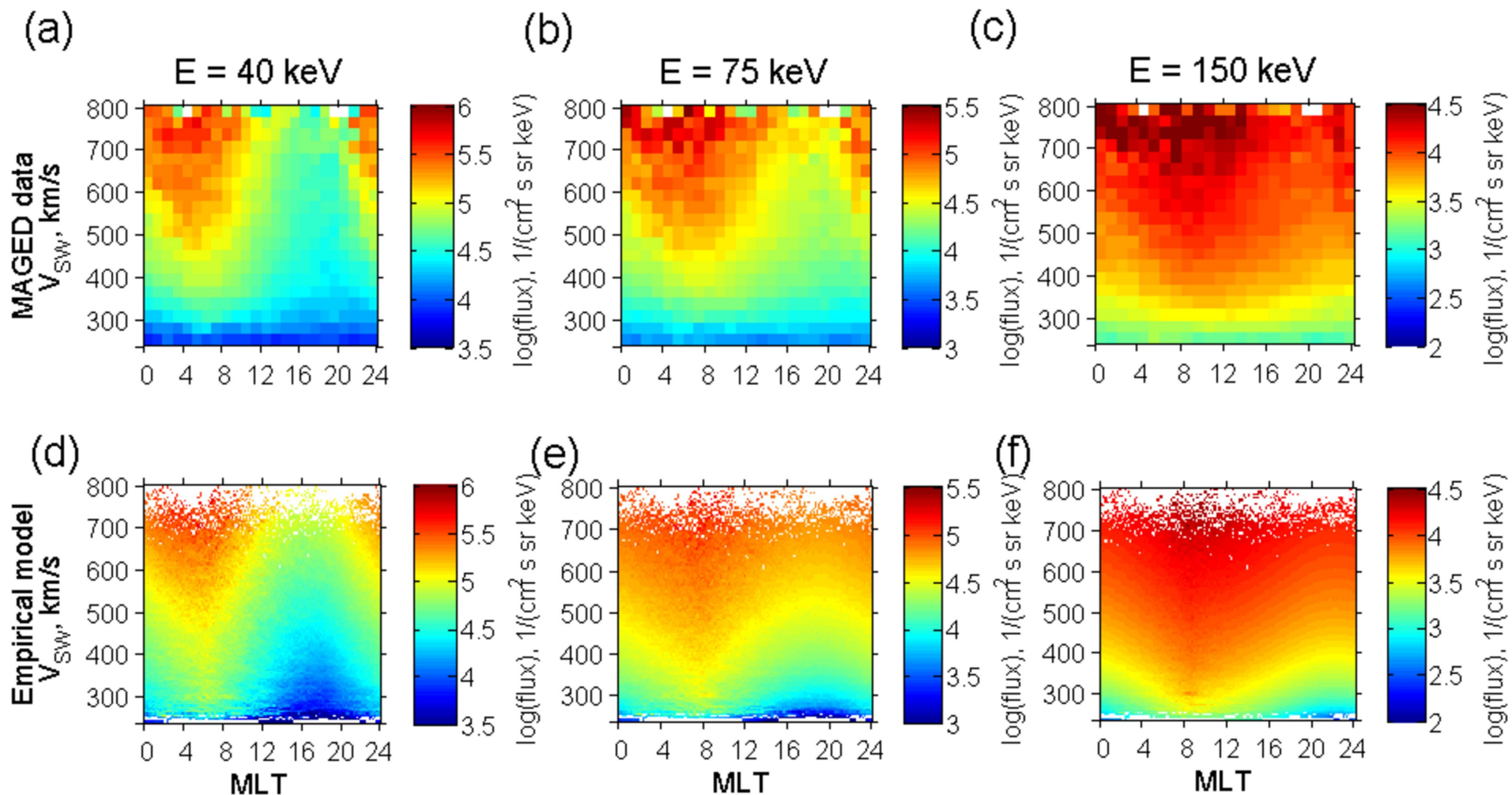
Author Manuscript



Author Manuscript



Author Manuscript



This article is protected by copyright. All rights reserved.